The Meridional Flow of Source-Driven Abyssal Currents in a Stratified Basin with Topography. Part II: Numerical Simulation

GORDON E. SWATERS

*Applied Mathematics Institute, Department of Mathematical and Statistical Sciences, and Institute for Geophysical Research,
University of Alberta, Edmonton, Alberta, Canada*

ABSTRACT

A numerical simulation is described for source-driven abyssal currents in a 3660 km × 3660 km stratified Northern Hemisphere basin with zonally varying topography. The model is the two-layer quasigeostrophic equations, describing the overlying ocean, coupled to the finite-amplitude planetary geostrophic equations, describing the abyssal layer, on a midlatitude β plane. The source region is a fixed 75 km × 150 km area located in the northwestern sector of the basin with a steady downward volume transport of about 5.6 Sv (Sv ≡ 10^6 m^3 s^{-1}) corresponding to an average downwelling velocity of about 0.05 cm s^{-1}. The other parameter values are characteristic of the North Atlantic Ocean. It takes about 3.2 yr for the abyssal water mass to reach the southern boundary and about 25 yr for a statistical state to develop. Time-averaged and instantaneous fields at a late time are described. The time-averaged fields show an equatorward-flowing abyssal current with distinct up- and downslope groundings with decreasing height in the equatorward direction. The average equatorward abyssal transport is about 8 Sv, and the average abyssal current thickness is about 500 m and is about 400 km wide. The circulation in the upper layers is mostly cyclonic and is western intensified, with current speeds about 0.6 cm s^{-1}. The upper layer cyclonic circulation intensifies in the source region with speeds about 4 cm s^{-1}, and there is an anticyclonic circulation region immediately adjacent to the western boundary giving rise to a weak barotropic poleward current in the upper layers with a speed of about 0.6 cm s^{-1}. The instantaneous fields are highly variable. Even though the source is steady, there is a pronounced spectral peak at the period of about 54 days. The frequency associated with the spectral peak is an increasing function of the downwelling volume flux. The periodicity is associated with the formation of transient cyclonic eddies in the overlying ocean in the source region and downslope propagating plumes and boluses in the abyssal water mass. The cyclonic eddies have a radii about 100–150 km and propagation speeds about 5–10 cm s^{-1}. The eddies are formed initially because of stretching associated with the downwelling in the source region. Once detached from the source region, the cyclonic eddies are phase locked with the boluses or plumes that form on the downslope grounding of the abyssal current, which themselves form because of baroclinic instability. Eventually, the background vorticity gradients associated with β and the sloping bottom arrest the downslope (eastward) motion, the abyssal boluses diminish in amplitude, the abyssal current flows preferentially equatorward, the upper layer eddies disperse and diminish in amplitude, and westward intensification develops.

---

1. Introduction

In a source region of deep water formation, the Sverdrup vorticity balance predicts equatorward abyssal flow (Stommel and Arons 1960). Away from the source region, Stommel–Arons theory cannot infer the flow direction of abyssal currents. However, many abyssal currents are characterized by the isopycnal field being grounded against sloping topography [e.g., the deep western boundary undercurrent in the North Atlantic Ocean (Richardson 1977), and the deep water replacement current in the Strait of Georgia (LeBlond et al. 1991; Masson 2002)] and the flow being in geostrophic balance. As shown by Nof (1983), a fully grounded abyssal water mass lying over sloping topography flows, in the fully nonlinear but reduced gravity dynamical limit, nondispersively and steadily in the along-slope direction, irrespective of the specific height or vorticity field within the abyssal water mass.

Corresponding author address: Gordon E. Swaters, Department of Mathematical and Statistical Sciences, University of Alberta, Edmonton, AB, T6G 2G1, Canada.
E-mail: gordon.swaters@ualberta.ca

These two results provide a dynamical scenario for the initiation and maintenance of source-driven grounded abyssal flow. That is, in high latitude regions where deep water is produced (often over sloping topography), the Sverdrup vorticity balance initiates equatorward flow. Once produced, this water mass can become grounded and geostrophically adjusted, maintaining a Nof balance that permits sustained basin-scale meridional quasi-steady and coherent abyssal flow.

Swaters (2006, hereinafter Part I) presented a hybrid quasigeostrophic–planetary geostrophic (QG–PG) three-layer baroclinic model that describes the formation and development of grounded abyssal currents as process that begins as a source-driven Stommel–Arons flow and then transitions to a Nof flow as the abyssal water mass flows equatorward. In particular, the subinertial evolution and equatorward flow of source-driven grounded abyssal currents over sloping topography and their baroclinic interaction with the overlying ocean on a midlatitude β plane was described. This model recovers the Stommel–Arons theory for the equatorward flow of a source-driven abyssal water mass (Stommel and Arons 1960), the nondispersive topographically steered inertial flow of a grounded abyssal water mass (Nof 1983), and the finite-amplitude β-induced westward propagation of abyssal water masses associated with the so-called planetary shock wave balance introduced by Anderson and Killworth (1979) and examined later by Dewar (1987), among others (see Part I), and the baroclinic instability between the grounded abyssal current on a sloping bottom and the overlying ocean (Swaters 1991).

Moreover, Part I introduced a new Stommel–Arons–Nof (SAN) nonlinear reduced-gravity steady-state balance that bridges both Stommel–Arons and Nof dynamics. This balance was explicitly solved to determine the meridional structure of an abyssal current that possesses cross-slope groundings (like that shown in Fig. 1). The theory predicted the equatorward thinning of the abyssal layer height (although the meridional transport is constant, i.e., the equatorward speed of the abyssal current increases in the equatorward direction) because of the conservation of abyssal PG potential vorticity. The influence of β is to (slightly) orient the pathlines in the northeast to southwest direction, that is, there is a cross-slope component in the abyssal velocity field. The solution does not correspond to a simple parallel shear flow.

In addition, Part I determined the baroclinic instability characteristics of the steady solutions. A variational principle was introduced for the baroclinic extension of all inertial solutions to the hybrid SAN model. This variational principle was exploited to establish (modal
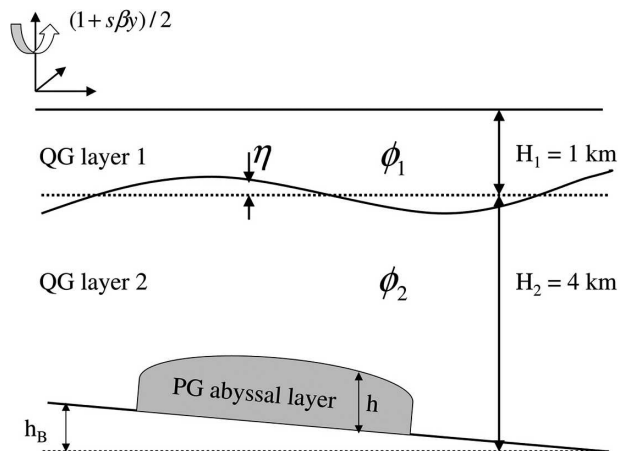

FIG. 1. Model geometry used in this paper.

and nonmodal) sufficient stability and necessary instability conditions. The linear baroclinic instability problem was solved for a constant (i.e., horizontally unsheared) velocity profile for the abyssal current with β and sloping topography present. The most unstable mode, for typical parameter values, corresponds to an equatorward- (or along-slope) propagating topographic Rossby wave with a wavelength on the order of 90 km, a period of about 38 days (the phase speed is about 3 cm s^{-1}), and an e-folding amplification time of about 6 days.

The principal purpose of this contribution to describe a numerical simulation of the fully coupled QG–PG model introduced in Part I for an idealized (steadily) source-driven grounded abyssal current on a sloping bottom in a 3660 km × 3660 km midlatitude β-plane basin centered at 40°N. The topography is an idealized (smoothly differentiable) representation of the actual meridional-averaged bottom bathymetry in the North Atlantic.

The plan of this paper is as follows. In section 2, the model equations are very briefly introduced and the values of the parameters used in the simulation are given. In section 3 the computational scheme is described. In particular, a novel upwelling scheme is introduced along the southern edge of the computational domain that allows the numerical simulation to evolve to a statistical steady state with respect to all the dynamical fields but, importantly, with respect to the total volume of abyssal water that exists in the domain (with rigid boundaries) even when the source is continuously turned on. It takes about 25 yr for the simulation to achieve a statistical steady state. The simulation described here is for a 40-yr period.

Section 4 describes the numerical simulation. Time-averaged fields, computed over the statistically steady

part of the simulation, and instantaneous fields, at a late time in the simulation, are described. There is considerable variability in the instantaneous fields as compared with the time-averaged fields. The paper is summarized in section 5.

2. Model equations

The model is an amalgamation, with the inclusion of variable topography and mass conserving up- and downwelling, of the two-layer quasigeostrophic (QG; i.e., Phillips) model used, for example, by Holland (1978) to investigate the baroclinic evolution of the wind-driven circulation and the QG–PG abyssal current model of Swaters (1991) describing the baroclinic instability of grounded abyssal flow on sloping topography. The reader is referred to Part I for a complete description of the underlying dynamical assumptions associated with the model derivation.

Assuming a Boussinesq, rigid-lid approximation with wind stress, horizontal and bottom friction, variable topography, and mass conserving up- or downwelling, the nondimensional model, in standard notation (see, e.g., Pedlosky 1987), can be written in the form

$$[\partial_t + J(\phi_1, \cdot)][\Delta\phi_1 - F_1(\phi_1 - \phi_2) + \beta y]$$

$$= \Upsilon\nabla \times \boldsymbol{\tau} + \frac{F_1 Q}{F_1 + F_2} + \frac{\Delta^2\phi_1}{R_e}, \qquad (2.1)$$

$$[\partial_t + J(\phi_2, \cdot)][\Delta\phi_2 - F_2(\phi_2 - \phi_1) + h + h_B + \beta y]$$

$$= -r_2\Delta\phi_2 + \frac{F_1 Q}{F_1 + F_2} + \frac{\Delta^2\phi_2}{R_e}, \quad \text{and} \qquad (2.2)$$

$$h_t + J\left(h + h_B + \phi_2, \frac{h}{1 + s\beta y}\right)$$

$$= Q + r_3\Delta(\phi_2 + h_B + h), \qquad (2.3)$$

with the auxiliary diagnostic relations

$$\mathbf{u}_{1,2} = \mathbf{e}_3 \times \nabla\phi_{1,2}, \quad \mathbf{u}_3 = \frac{\mathbf{e}_3 \times \nabla(\phi_2 + h_B + h)}{1 + s\beta_y},$$

$$p = \phi_2 + h_B + h \quad \text{and} \quad \eta = \phi_2 - \phi_1, \qquad (2.4)$$

where subscript 1, 2, or 3 on a physical variable refers to the upper, middle, and abyssal layer, respectively; alphabetical subscripts (unless otherwise noted) indicate partial differentiation, $\mathbf{u}_{1,2,3} = (u_{1,2,3}, v_{1,2,3})$, h_B is the height of the topography, h is the height of the abyssal layer relative to h_B, η is the deflection (measured positively upward) of the interface between the two QG layers from its equilibrium position, $\boldsymbol{\tau}$ is the wind stress,

and Q is the down- and/or upwelling term, respectively. The dynamic pressures in the upper two layers are given by $\phi_{1,2}$, and in the abyssal layer by p. The model geometry is shown in Fig. 1. The last two equations in (2.4) express the continuity of total pressure across the deforming interfaces between the middle and abyssal layers, and the upper and middle layers, respectively.

The dynamical parameters in the model are defined by

$$s = \frac{s^* L}{H_2}, \quad \beta = \frac{\beta^* L^2}{U_*}, \quad R_e = \frac{U_* L}{A_H}, \quad \Upsilon = \frac{\Upsilon^* L}{\rho_* H_1 U_*^2},$$

$$F_1 = \frac{g' H_2}{\tilde{g} H_1}, \quad F_2 = \frac{g'}{\tilde{g}}, \quad \text{and} \quad r_{2,3} = \frac{r_{2,3}^*}{s H_2}, \qquad (2.5)$$

where $H_{1,2}$ are the constant reference layer thicknesses in the upper two layers, ρ_* is the reference Boussinesq density, $g' = (\rho_3 - \rho_2)g/\rho_* > 0$ and $\tilde{g} = (\rho_2 - \rho_1)g/\rho_* > 0$, where $\rho_{1,2,3}$ correspond to the constant density in each individual layer with $0 < \rho_1 < \rho_2 < \rho_3$, $L = \sqrt{g' H_2}/f_0$ (the internal deformation radius for the middle layer based on the density difference with the abyssal layer), $U_* = s^* g'/f_0$ (the Nof speed), $s^* \approx O(\nabla^* h_B^*)$ (a representative value for the topographic slope), f_0 is the reference Coriolis parameter, β^* is the northward gradient of the Coriolis parameter, and Υ^* is a typical value for the wind stress.

In addition, A_H is the upper QG layers' horizontal eddy coefficient and $r_{2,3}^*$ are bottom friction coefficients for the middle and abyssal layers, respectively. Ekman boundary layer theory (Pedlosky 1987) suggests that $r_{2,3}^*$ are the scale vertical thicknesses of the Ekman bottom boundary layer in the middle and abyssal layers, respectively.

The upwelling/downwelling parameterization (the Q terms) is introduced in such a way as ensure that in the unforced, inviscid limit, the horizontal divergence of the barotropic mass flux is zero (see the appendix in Part I). That is, whatever mass is accumulated into or lost from the abyssal layer is assumed to have been instantaneously gained from or lost into the upper two layers in proportion to the individual upper layer volume fractions. Total volume is conserved in the unforced, inviscid limit of the model equations. The net horizontal divergence of the barotropic mass transport is forced only by wind stress and bottom friction. The unforced, inviscid dynamics of the model is, therefore, purely baroclinic. Equations (2.1), (2.2), and (2.3) can be formally derived in a small Rossby number limit (i.e., $s \to 0$; see the appendix in Part I) of the three-layer shallow water equations using the scaling arguments of Swaters (1991).

Although there is considerable variability, typical basin-scale values of the physical parameters are

$$\tilde{g} \simeq 9.5 \times 10^{-3} \text{ m s}^{-2}, \quad g' \simeq 4.8 \times 10^{-4} \text{ m s}^{-2},$$
$$s^* \simeq 5.6 \times 10^{-3}, \quad \Upsilon^* \simeq 10^{-1} \text{ N m}^{-2},$$
$$H_1 \simeq 1 \text{ km}, \quad A_H \simeq 1.6 \times 10^{4} \text{ m}^2 \text{ s}^{-1},$$
$$H_2 \simeq 4 \text{ km}, \quad f_0 \simeq 9.35 \times 10^{-5} \text{ s}^{-1}, \quad \text{and}$$
$$\beta^* \simeq 1.6 \times 10^{-11} \text{ (ms)}^{-1}, \tag{2.6}$$

which implies that

$$L \simeq 15 \text{ km}, \quad U_* \simeq 3 \text{ cm s}^{-1},$$

$$T \equiv \frac{Lf_0}{s^*g'} \simeq 6 \text{ days},$$
$$(H_3, h_B^*) \equiv s^*L \simeq 84 \text{ m}, \quad \text{and}$$
$$Q_* \equiv s^{*2}g'/f_0 \simeq 1.6 \times 10^{-2} \text{ cm s}^{-1}, \tag{2.7}$$

where T, Q_*, H_3, and h_B^* are the formal scalings for the time, upwelling/downwelling mass exchange between the abyssal layer and the overlying ocean, abyssal, and topographic height used in the derivation of (2.1), (2.2), and (2.3), respectively. The rotational parameters f_0 and β^* have been evaluated at 40°N (the origin of the computational domain). These scalings imply that the nondimensional parameters are about

$$s \simeq 0.02, \quad F_1 \simeq 0.2, \quad F_2 \simeq 0.05, \quad r_2 \simeq 0.08,$$
$$\beta \simeq 0.12, \quad R_e \simeq 1/35, \quad \Upsilon \simeq 1.62, \quad \text{and} \quad r_3 \simeq 0.001. \tag{2.8}$$

In this paper, the source-driven $Q \neq 0$ with no wind stress $\Upsilon = 0$ limit is considered. In a forthcoming contribution, the dynamical coupling between the surface-intensified wind- and source-driven abyssal circulations will be examined. The parameters $r_{2,3}$ are chosen so that bottom friction will not play a dominant role in the numerical simulations. It follows from (2.8) that $r_3^* \simeq O(1 \text{ m})$ and $r_2^* \simeq O(10 \text{ m})$, which corresponds to very thin bottom boundary layers.

3. The computational scheme

Equations (2.1), (2.2), and (2.3) were numerically solved as the system

$$[\partial_t + J(\phi_1, \cdot)](q_1 + \beta y) = \frac{F_1 Q}{F_1 + F_2} + \frac{\Delta^2 \phi_1}{R_e} - \nu_N \Delta^3 \phi_1, \tag{3.1}$$

$$[\partial_t + J(\phi_2, \cdot)](q_2 + h_B + \beta y)$$
$$= \frac{F_1 Q}{F_1 + F_2} - r_2 \Delta \phi_2 + \frac{\Delta^2 \phi_2}{R_e} - \nu_N \Delta^3 \phi_2, \tag{3.2}$$

$$h_t + J\left(h + h_B + \phi_2, \frac{h}{1 + s\beta y}\right)$$
$$= Q + \chi_h r_3 \Delta(\phi_2 + h_B + h), \tag{3.3}$$

$$\Delta \phi_1 - F_1(\phi_1 - \phi_2) = q_1, \quad \text{and} \tag{3.4}$$

$$\Delta \phi_2 - F_2(\phi_2 - \phi_1) = q_2 - h, \tag{3.5}$$

in a 40° × 40° (extending from 20° to 60°N), or equivalently, an approximately 3660 km × 3660 km (or, nondimensionally, a 244 × 244) square basin, denoted by Ω, and given by

$$\Omega = [(x, y) | x_W < x < x_E \quad \text{and} \quad y_S < y < y_N], \tag{3.6}$$

where $-x_W = x_E = -y_S = y_N = 122.0$ and χ_h is the characteristic function associated with h [i.e., $\chi_h = 1$ if $h > 0$ and $\chi_h = 0$ otherwise; note that $h \geq 0$ for all (x, y, t)].

Equations (3.1), (3.2), and (3.3) were integrated forward in time using a 513 × 513 second-order-accurate leapfrog procedure with the Arakawa (1966) finite-difference scheme implemented for the Jacobian. The grid spacing is $\delta_x \equiv 244/512$ (corresponding dimensionally to about 7 km) and the time step is $\delta_t \equiv 1.25 \times 10^{-3}$ (corresponding dimensionally to about 10 min). A Robert filter (Asselin 1972) with coefficient 5.0×10^{-3} was applied at each time step to suppress the computational mode. Additionally, weak ($\nu_N = 5 \times 10^{-8}$) biharmonic friction is introduced into (3.1) and (3.2) to suppress high wavenumber noise. The simulations were computationally stable. The parameters s, β, $F_{1,2}$, R_e, and $r_{2,3}$ are given by (2.8). The initial conditions are $h = \phi_{1,2} = 0$ at $t = 0$.

The numerical implementation of the boundary conditions is somewhat subtle. Because there is horizontal friction in the QG layers, the no slip conditions $\nabla \phi_{1,2} = \mathbf{0}$ are imposed for all $t \geq 0$ on the boundary of the domain Ω; that is, the side walls, henceforth denoted by $\partial\Omega$. The updated values of the QG-relative vorticities, $\Delta\phi_{1,2}$, on $\partial\Omega$, required in time stepping (3.1) and (3.2) (because of the presence of the horizontal friction terms), are determined by the finite difference implementation of Chorin's vorticity creation scheme (Orszag and Israeli 1974; Hou and Wetton 1992). Along the boundaries, the derivatives associated with the numerical biharmonic friction terms in (3.1) and (3.2) were evaluated with one-sided second-order accurate finite differences. For the abyssal layer, which does not

have horizontal friction (see the appendix in Part I), the appropriate boundary condition, for an impermeable $\partial\Omega$ associated with the bounded simply connected domain Ω, will be the Dirichlet condition $h = 0$ on $\partial\Omega$ for all $t \geq 0$ (the support of h does not intersect $\partial\Omega$).

The appropriate Dirichlet condition for the QG streamfunctions, $\phi_{1,2}$, on $\partial\Omega$, are that they are functions of time, chosen so that the vertical velocity on the interface between the upper two layers satisfies the area-averaged continuity constraint (McWilliams 1977)

$$\int\int_\Omega w_{1,2|z=H_2}\, dx\, dy = \frac{\partial}{\partial t}\int\int_\Omega \phi_2 - \phi_1\, dx\, dy$$

$$= \frac{1}{F_1 + F_2}\int\int_\Omega Q\, dx\, dy, \quad (3.7)$$

which follows from the shallow water continuity equations used to derive (3.1)–(3.5) (see the appendix in Part I).

A straightforward variant of McWilliams's (1977) and Holland's (1978) procedure for solving the elliptic equations in (3.4) and (3.5) subject to (3.7) is imple-

mented. Introducing the baroclinic (BC) and barotropic (BT) QG streamfunctions

$$\psi_{BC} \equiv \phi_2 - \phi_1 \quad \text{and} \quad \psi_{BT} \equiv (F_2\phi_1 + F_1\phi_2)/(F_1 + F_2)$$
$$(3.8)$$

into (3.4) and (3.5), respectively, leads to

$$(\Delta - F_1 - F_2)\psi_{BC} = \mathcal{F}_{BC} \equiv q_2 - q_1 - h \quad \text{and} \quad (3.9)$$
$$\Delta\psi_{BT} = \mathcal{F}_{BT} \equiv [F_2q_1 + F_1(q_2 - h)]/$$
$$(F_1 + F_2), \quad (3.10)$$

where ψ_{BT} is obtained by inverting (3.10), using a direct solver, subject to $\psi_{BT} = 0$ on $\partial\Omega$. To determine ψ_{BC}, the decomposition

$$\psi_{BC}(x, y, t) = \psi_P(x, y, t) + \delta(t)\psi_H(x, y) \quad (3.11)$$

is introduced, where

$$(\Delta - F_1 - F_2)\psi_P = \mathcal{F}_{BC}, \quad \text{with} \quad \psi_P = 0 \quad \text{on} \quad \partial\Omega,$$
$$(3.12)$$

and

$$(\Delta - F_1 - F_2)\psi_H = 0, \quad \text{with} \quad \psi_H = 1 \quad \text{on} \quad \partial\Omega,$$
$$(3.13)$$

from which it follows from (3.7) that

$$\delta(t) = \frac{\int\int_\Omega\left[\int_0^t Q(x, y, \xi)\, d\xi\right] dx\, dy - (F_1 + F_2)\int\int_\Omega \psi_P(x, y, t)\, dx\, dy}{(F_1 + F_2)\int\int_\Omega \psi_H(x, y)\, dx\, dy}, \quad (3.14)$$

(δ is a time-dependent coefficient and not the Dirac delta function). The numerical integration itself ensures that the appropriate mass balance relationship associated with the abyssal layer height is respected.

The PG equation in (2.3) permits grounded abyssal currents that possess the property that h can intersect the bottom along a specific curve(s), denoted generically by $\varphi(x, y, t) = 0$. Swaters (1991) has shown that (2.3) is itself the appropriate kinematic and dynamic boundary condition for h on the grounding $\varphi(x, y, t) = 0$. This means that, when a grounding is present, the solution of (2.3) automatically determines the correct evolution and placement of the groundings [note that $h \equiv 0$ solves (2.3)]. No additional matching, continuity or boundary conditions for h are required at or across the groundings, or are needed to determine, formally, $\varphi(x, y, t) = 0$. This is a noteworthy feature of the QG–PG model (2.1), (2.2), and (2.3).

With respect to the bottom topography h_B, the ob-

jective was to use a representation that is not inconsistent with the zonal structure of the real topography but that is sufficiently idealized that the spatial and temporal variability seen in the simulation is the consequence of internal dynamics in the model and is not generated by poorly represented orography. It is important to emphasize that the numerical integration being described here is not to be considered a real oceanographic simulation with the vast array of more-or-less accurate physics like that presumed to be associated with ocean general circulation models, but a highly idealized theoretical process study intended to explore the implications of the model dynamics for grounded abyssal flow like the deep western boundary currents.

The modeled bottom topography was obtained by averaging, along meridional paths that are a fixed distance from the North American coast, over the latitude band 20°–60°N, extending 40° longitudinally eastward from the North American coast at each latitude (U.S.

Naval Oceanographic Office's digital bathymetric data, available online at https://idbms.navo.navy.mil). This is a conformal mapping procedure that maps data from a nonrectangular geographical region onto the square domain Ω where $x = x_W$ corresponds to the coastline. From the meridionally averaged bathymetry so obtained, a smooth idealized zonally varying profile was extracted that eliminates the beginnings of the rise associated with the Mid-Atlantic Ridge.

Figure 2a shows the result. The dashed line in Fig. 2a is the "real" bottom topography as obtained by the averaging procedure described above. Recall that h_B is nondimensional and is the height of the bottom topography relative to a depth of 5 km scaled by $s^*L \simeq 84$ m (where s^* and L are a representative bottom slope and the internal deformation radius associated with the middle QG layer using the density difference with the abyssal layer, respectively). The solid line in Fig. 2a is the (smoothly differentiable) idealized bottom topography used in the numerical simulation and is given by

$$h_B(x) = \gamma_1 + \gamma_2\left[\sqrt{\gamma_3 + (x - x_0)^2} - (x - x_0)\right], \quad (3.15)$$

where the parameters $\gamma_{1,2,3}$ and x_0 are subjectively chosen to approximate the meridionally averaged bathymetry as closely as possible and are given by $\gamma_1 = -58.16$, $\gamma_2 = 0.58$, $\gamma_3 = 200.0$, and $x_0 = -69.5$. The representation (3.15) for $h_B(x)$ possesses the property that $h'_B(x) \simeq -1$ for $x \ll x_0$ and $h'_B(x) \simeq 0$ for $x \gg x_0$ with the transition occurring at $x = x_0$.

Another aspect that needs to be described is the implementation of the up- and/or downwelling term $Q(x, y, t)$. The source region for the abyssal water will be in the northwest corner of the computational domain and is located, in nondimensional variables, in the region

$$\Omega_{\text{down}} = [(x, y)| |x + 110.0| < 2.5 \quad \text{and} \quad |y - 109.5| < 5.0],$$
$$(3.16)$$

with the steady source in this region given by

$$Q_{\text{down}}(x, y) = \begin{cases} \dfrac{\mathcal{H}_{\text{down}}}{2}\left\{1 + \cos\left[\dfrac{\pi(y - 109.5)}{5.0}\right]\right\}, & \text{if} \quad (x, y) \in \Omega_{\text{down}}, \\ 0, & \text{otherwise,} \end{cases} \quad (3.17)$$

where $\mathcal{H}_{\text{down}} = 6.0$. This implies an average dimensional downwelling velocity of about 0.05 cm s^{-1} and an average downward volume transport of about 5.6 Sv (Sv $\equiv 10^6$ m^3 s^{-1}) over the region Ω_{down}. The source region, Ω_{down}, has an area of about 11 250 km^2, and extends about 75 km zonally and about 150 km meridionally (i.e., about 0.8° zonally and 1.6° meridionally) and is located far enough away from the western and northern boundaries, located at $x = x_W$ and $y = y_N$, respectively, so that the boundaries will not immediately affect the flow evolution. Numerical experimentation was done to choose the dimensions of Ω_{down} and the magnitude of $\mathcal{H}_{\text{down}}$. The objective was to have a source region and strength that resulted in an abyssal current with a cross-slope extent and along-slope transport that was not completely inconsistent with observations in the northwest Atlantic.

The source term implemented in this simulation is steady. It would, of course, be oceanographically relevant to examine the abyssal current produced with seasonal variations included in Q_{down}. As will be shown, even with a steady source term there will be time variability in the simulations at a specific frequency. It is important to separate out the time variability that arises from the internal dynamics of the model from that which might arise from seasonal variations in Q_{down}.

Pavec et al. (2005) and Ha and Swaters (2006) have recently shown that time variations in the abyssal current velocity can have a profound effect on the baroclinic instability properties (see, also, Pedlosky and Thomson 2003). The examination of the effect of seasonal variability in buoyancy-driven grounded abyssal currents is an important study that will be left for a future paper.

Once the abyssal water mass is formed it will flow equatorward on the sloping topography and will eventually encounter the southern boundary located at $y = y_S$. Rather than implement a porous southern boundary, an upwelling region immediately adjacent to y_S was introduced in such a manner as to ensure that a steady state develops in the total mass or volume of abyssal water that exists in the computational domain. The advantage of this procedure is that it allows the implementation of Dirichlet boundary conditions for the QG stream functions and abyssal height and allows (3.7) to be satisfied unambiguously.

As the numerical integration proceeds, baroclinic interactions between the abyssal water mass and the overlying water column lead to the formation of abyssal plumes or boluses that form on the downslope grounding in the abyssal height. Depending on the simulation parameters, some of these plumes can penetrate into
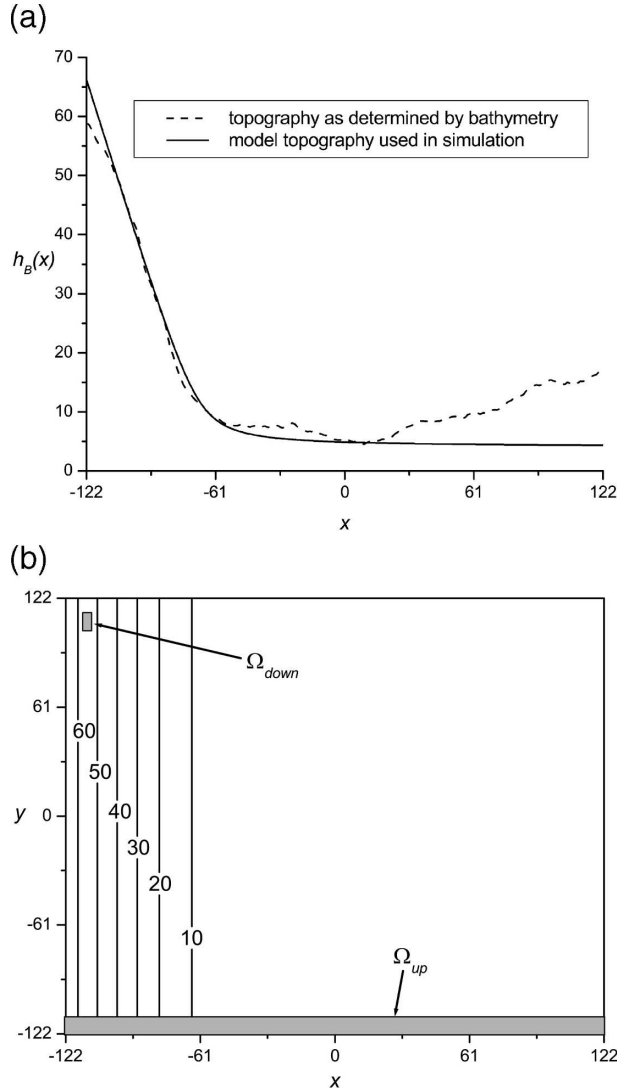
(a)

(b)

FIG. 2. (a) Bottom topography used in this paper; $h_B = 1$ corresponds to about 84 m and the horizontal length scale is about 15 km. (b) Plan view of the computational domain Ω. The contour lines are isobaths of h_B. The source region Ω_{down} (in the northwest corner) and the upwelling region Ω_{up} (immediately adjacent to the southern boundary) are shown as gray-shaded areas and are drawn to scale.

the region where the slope of the topography is effectively zero. In this flat-bottomed region, the abyssal water mass is no longer forced equatorward due to the Nof balance and can be, as it turns out, advected northward by the weak mean flow generated in the upper QG layers (looking rather like a poleward cyclonic recirculation in the eastern region of the domain). Rather than have this portion of the abyssal water mass accumulate along the northern boundary of the domain over decades of numerical integration, it was decided to also implement the upwelling scheme for these recirculating streamers. It is noted that if the topography does not flatten out, or if the downwelling volume flux in the source region is not sufficiently strong enough, or if β is sufficiently large enough, these recirculating abyssal streamers do not form.

Numerical experimentation showed that irrespective of the particular values associated with Ω_{down} and Q_{down} it took about 200 nondimensional time units (or, dimensionally, about 3.2 yr) for the equatorward flowing grounded abyssal water mass to reach the southern boundary. The reason that the time to reach the southern boundary is not strongly dependent on the source parameters is that, once formed, the meridional or along-continental slope motion is strongly governed by the nondispersive Nof (1983) balance (see Part I).

The southern upwelling region was implemented as follows. The upwelling region is given by

$$\Omega_{\text{up}} = [(x, y) | x_W < x < x_E \quad \text{and} \quad y_S < y < y_{\text{UP}}],$$

(3.18)

where $y_{\text{UP}} = -112.0$ (dimensionally, the north–south extent of the upwelling zone is about 150 km). Figure 2b shows the integration domain Ω with the nondimensional isobaths contoured and with the source region Ω_{down} and the upwelling region Ω_{up} marked as shaded areas, respectively.

For $0 \leq t < 200$ there is no upwelling along the southern boundary since there is very little abyssal water in Ω_{up}. For $t \geq 200$, the time-dependent upwelling parameterization

$$Q_{\text{up}}(x, y, t) = \begin{cases} -\dfrac{\mathcal{H}_{\text{up}}(t)h(x, y, t)}{2} \left\{ 1 + \cos\left[\dfrac{\pi(y - y_S)}{(y_{\text{UP}} - y_S)} \right] \right\}, & \text{if} \quad (x, y) \in \Omega_{\text{up}}, \\ 0, & \text{otherwise}, \end{cases}$$

(3.19)

is introduced, where $\mathcal{H}_{\text{up}}$ is chosen so that there is no further net mass accumulation in the abyssal layer for $t \geq 200$, that is,

$$\iint\limits_{\Omega_{\text{down}}} Q_{\text{down}}(x, y) \, dx \, dy + \iint\limits_{\Omega_{\text{up}}} Q_{\text{up}}(x, y, t) \, dx \, dy = 0,$$

(3.20)

so that

$$\mathcal{H}_{up}(t) = \begin{cases} \dfrac{\displaystyle\iint\limits_{\Omega_{down}} Q_{down}(x, y)\, dx\, dy}{\displaystyle\iint\limits_{\Omega_{up}} \dfrac{h(x, y, t)}{2}\left\{1 + \cos\left[\dfrac{\pi(y - y_S)}{(y_{UP} - y_S)}\right]\right\} dx\, dy} \geq 0, & \text{if } t \geq 200, \\[30pt] 0, & \text{otherwise.} \end{cases} \tag{3.21}$$

As will be shown later, the upwelling parameterization ensures that the numerical integration evolves to a statistical steady state. However, numerical experimentation also showed that the upwelling parameterization (3.19), which corresponds to Rayleigh-like damping in Ω_{up}, allowed Gibbs oscillations to develop in $h(x, y, t)$ in Ω_{up} as $h(x, y, t) \to 0$ as $y \downarrow y_S$. These unphysical oscillations were smoothly and effectively removed by the introduction of a sponge layer in Ω_{up}, in which the scale selective damping term

$$\frac{(1 - r_3)}{2}\left\{1 + \cos\left[\frac{\pi(y - y_S)}{(y_{UP} - y_S)}\right]\right\}\Delta h,$$

$$\text{if } (x, y) \in \Omega_{up}, \quad \text{and} \quad 0, \quad \text{otherwise,} \tag{3.22}$$

was added to the right-hand side of (3.3).

Thus, in summary, Q is given by

$$Q \equiv Q_{down}(x, y) + Q_{up}(x, y, t), \tag{3.23}$$

where Q_{down} and Q_{up} are given by (3.17) and (3.19), respectively, with $\mathcal{H}_{up}$ given by (3.21). Note that since (3.20) implies that

$$\iint\limits_{\Omega} Q\, dx\, dy = 0, \quad \text{for} \quad t \geq 200, \tag{3.24}$$

the first term in the numerator in (3.14) will be constant, or, equivalently, the right-hand term in (3.7) will be zero for $t \geq 200$.

Last, the numerical integration was done over the interval $t \in (0, 2500]$ (corresponding to a dimensional integration period of about 40 yr). This was sufficient time for a statistical steady state to develop. The numerical integrations took about 30 days on a 4-CPU Silicon Graphics, Inc., (SGI) Origin 350. The overwhelming majority of the CPU cycles were used in inverting (3.9) and (3.10). The forward integrations of (3.1), (3.2), and (3.3) consumed, comparatively, very few cycles. Typically, the data from the simulation were archived every 8000 time steps, or about every 60 simulation days. However, in some simulations, the data were archived every 6 or 12 days depending on the resolution needed in the data time series.

4. Description of the simulation

a. Area-averaged diagnostics

Figures 3a–d show, respectively, the area-averaged nondimensional energy E given by

$$E(t) = \frac{1}{2}\iint\limits_{\Omega} \{F_2\nabla\phi_1 \cdot \nabla\phi_1 + F_1[\nabla\phi_2 \cdot \nabla\phi_2 + (h + h_B)^2 - h_B^2] + F_1F_2(\phi_1 - \phi_2)^2\}\, dx\, dy, \tag{4.1}$$

the nondimensional total abyssal volume $\text{Vol}_{abyssal}$ given by

$$\text{Vol}_{abyssal}(t) = \iint\limits_{\Omega} h\, dx\, dy, \tag{4.2}$$

the nondimensional abyssal volume in the southern upwelling zone Vol_{up} given by

$$\text{Vol}_{up}(t) = \iint\limits_{\Omega_{up}} h\, dx\, dy, \tag{4.3}$$

and the upwelling coefficient, $\mathcal{H}_{up}$, as given by (3.21), versus the dimensionalized integration time t^* in units of years. In the absence of wind forcing, interlayer mass exchange and dissipation (i.e., $\Upsilon = Q = r_{2,3} = 0, R_e \to \infty$), it follows that $dE/dt = d(\text{Vol}_{abyssal})/dt = 0$. In the unforced limit, (2.1), (2.2), and (2.3) is an infinite-dimensional Hamiltonian dynamical system (see Part I; Swaters 1993), in which E will be the Hamiltonian functional.

Figure 3a shows the relatively rapid increase in E in the interval $0 \leq t^* \lesssim 3.2$ yr, at which time the upwelling
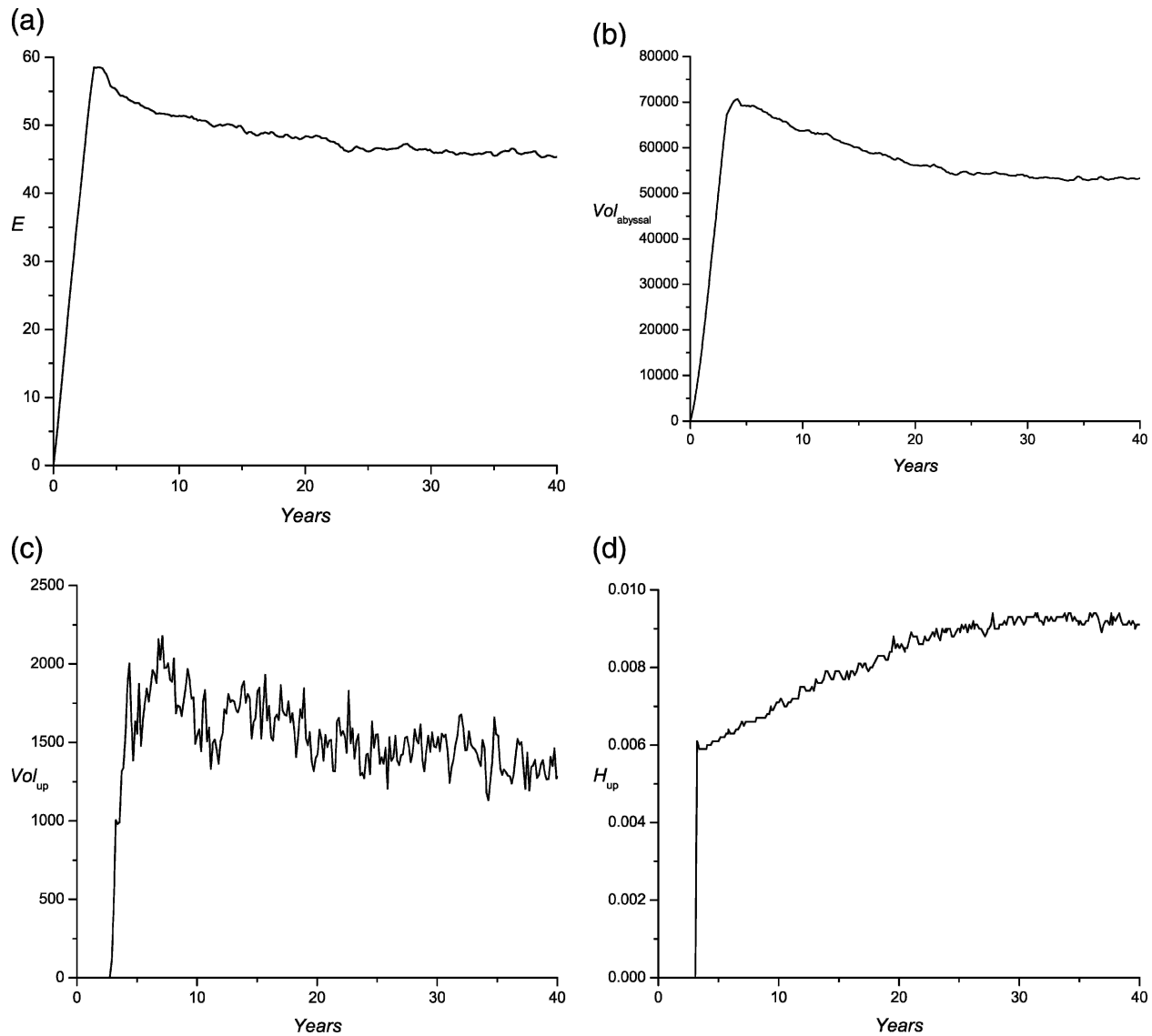
FIG. 3. (a) Area-averaged energy E, (b) abyssal volume in the full integration domain Ω, (c) abyssal volume in the upwelling region $\Omega_{\rm up}$, and (d) upwelling coefficient $\mathcal{H}_{\rm up}$ vs integration (yr).

along the southern boundary commences and the evolution toward steady state begins. For $t^* \gtrsim 3.2$, there is a gradual decrease in E that eventually levels off at, or asymptotes toward $E \simeq 45$, associated, primarily, with the development of a steady state in the abyssal volume and potential energy. The area-averaged abyssal potential energy, with energy density proportional to h^2 (and not shown here) shows exactly the same qualitative behavior as that seen in Fig. 3a.

Figure 3b shows $\mathrm{Vol}_{\rm abyssal}$ versus t^*. Dimensionally, $\mathrm{Vol}_{\rm abyssal} = 1$ is equivalent to a volume of about 18.9 km^3 of abyssal water. Initially, there is no abyssal water, of course, anywhere in Ω and $\mathrm{Vol}_{\rm abyssal}$ rapidly increases over the integration period $0 \leq t^* \lesssim 3.2$ yr,

when there is no upwelling. Once upwelling starts along the southern boundary, there is a gradual decrease in the volume of abyssal water that eventually asymptotically approaches about $\mathrm{Vol}_{\rm abyssal} \simeq 53\,000$, which is dimensionally equivalent to about 10^{15} m^3. This volume is spread over a 40° latitude band. Numerically, it takes about 25 yr to reach this steady state from rest.

Figure 3c shows the time development of the (nondimensional) volume of abyssal water, $\mathrm{Vol}_{\rm up}$, in the upwelling region $\Omega_{\rm up}$. Dimensionally, $\mathrm{Vol}_{\rm up}$ scales the same as $\mathrm{Vol}_{\rm abyssal}$. For $0 \leq t^* \lesssim 3.2$ yr, no abyssal water has entered $\Omega_{\rm up}$. Subsequently, even though upwelling has been initiated, there is an interval of time when there is a very rapid increase in the volume of abyssal

water in Ω_{up}, as abyssal water continues to flow into the region. Eventually, once upwelling has been numerically initiated, the volume of abyssal water in Ω_{up} gradually declines, eventually oscillating about a constant value given by $Vol_{up} \simeq 1400$, which is dimensionally equivalent to about $26 \times 10^{12} \ m^3$. The simulations suggest that the abyssal water is preferentially located in the $x_W < x \leq -62$ subregion of the 150-km-wide latitude band Ω_{up}.

The variability in Vol_{up}, as seen in Fig. 3c, is a consequence of the strong baroclinic interactions that occur between the abyssal water mass and the overlying ocean as the abyssal water mass flows equatorward. A power spectrum analysis of the detrended signal seen in Fig. 3c (not shown here) suggests that there is no single dominant periodicity in the oscillatory signal seen in Vol_{up}.

Figure 3d shows the evolution of the upwelling coefficient $\mathcal{H}_{up}$ over the numerical integration. In the interval $0 \leq t^* \lesssim 3.2$ yr, $\mathcal{H}_{up} \equiv 0$ as there is no upwelling. The moment the upwelling begins, there is discontinuous change in $\mathcal{H}_{up}$ as it jumps from 0 to about 0.006. After upwelling has begun, $\mathcal{H}_{up}$ gradually increases and eventually levels off at a value of about 0.009.

A characteristic value or bulk estimate of the (upward) nondimensional vertical velocity in Ω_{up} associated with the upwelling parameterization is given by

$$w_{up} \approx \mathcal{H}_{up}(t) \times Vol_{up}(t) \bigg/ \iint_{\Omega_{up}} \chi_h \, dx \, dy. \quad (4.4)$$

Once the steady state has developed, $w_{up} \approx O(10^{-3})$ which, dimensionally, implies $w_{up}^* \approx O(10^{-5})$ cm s^{-1}. The vertical velocity associated with the upwelling region Ω_{up} is much smaller, in absolute value, than the vertical downwelling velocity associated with the source region Ω_{down} because the area of the source region is much smaller than the area that the upwelling takes place over [which is the integral in the denominator in (4.4)]. Once upwelling has been started in the simulation, since (3.20) holds, the upward transport in Ω_{up} exactly balances the downward transport in Ω_{down}.

In summary, Fig. 3 suggests that the upwelling scheme introduced here does a reasonably good job of allowing a statistical steady state to develop in the total volume of abyssal water in the domain Ω in the simulation. The great advantage of this scheme is that it can be introduced into a reduced shallow water model (with its underlying hydrostatic assumptions) and into a domain with fixed boundaries with time-varying Dirichlet conditions as required to satisfy (3.7).

b. Time-averaged fields

Time-averaged fields, denoted by an overbar, were computed over the last 15 yr of the simulation and are given by

$$(\bar{\phi}_1, \bar{\phi}_2, \bar{h})(x, y) \equiv \frac{1}{15} \int_{25}^{40} (\phi_1, \phi_2, h) \, dt^*, \quad (4.5)$$

with corresponding definitions for $\bar{\psi}_{BC}$ and $\bar{\psi}_{BT}$. In terms of the nondimensional time t, the averaging interval is $t \in [1560, 2500]$. The averaging interval was chosen subjectively on the basis that it was the largest interval of time in which adding or deleting a few years from the interval did not dramatically change the results and is consistent with Fig. 3.

Figures 4a and 4b show contour plots of the time-averaged nondimensional QG barotropic streamfunction $\bar{\psi}_{BT}$ and the dimensional abyssal height $\bar{h}^* \equiv (s^*L)\bar{h}$, respectively, for the western half of the computational domain (the fields are essentially zero on the eastern side of the computational domain). Because it is the spatial pattern and gradient of the QG streamfunction, rather than the precise dimensional value, which are most important in this study, $\bar{\psi}_{BT}$ is shown nondimensionally. However, since the dimensional height of the abyssal current is of interest, it is contoured in meters. The axes remain nondimensional and it is remarked, since the length scale is 15 km, that the zonal extent and meridional extent of the region shown in Figs. 4a,b are 1800 and 3660 km, respectively.

The positive and negative values of $\bar{\psi}_{BT}$ in Fig. 4a are contoured with solid and dashed lines, respectively, and the contour interval is ± 0.8. The pattern for $\bar{\psi}_{BT}$ corresponds to a broad, westward-intensified, cyclonic circulation over the entire domain, except for a region of anticyclonic circulation located immediately adjacent to the western boundary (which is more completely described below). There is a relatively strong localized cyclonic circulation subregion in Ω_{down}, resulting from the stretching associated with the downwelling that forms the abyssal water mass. The minimum in $\bar{\psi}_{BT}$ is located at the center of Ω_{down} (i.e., at $x = -110$ and $y = 109.5$) and has a value of about -9.5. The barotropic QG velocities associated with the localized circulation in Ω_{down} have a dimensional magnitude of about 4 cm s^{-1}.

Away from Ω_{down}, the cyclonic circulation weakens but nevertheless extends meridionally throughout the domain. Typical current speeds associated with the southward flow along the boundary with the anticyclonic cell (i.e., the region approximately given by $-107 < x < 92$ and $-60 < y < 61$) are about 0.6 cm s^{-1}. These speeds decrease to zero as one moves into the
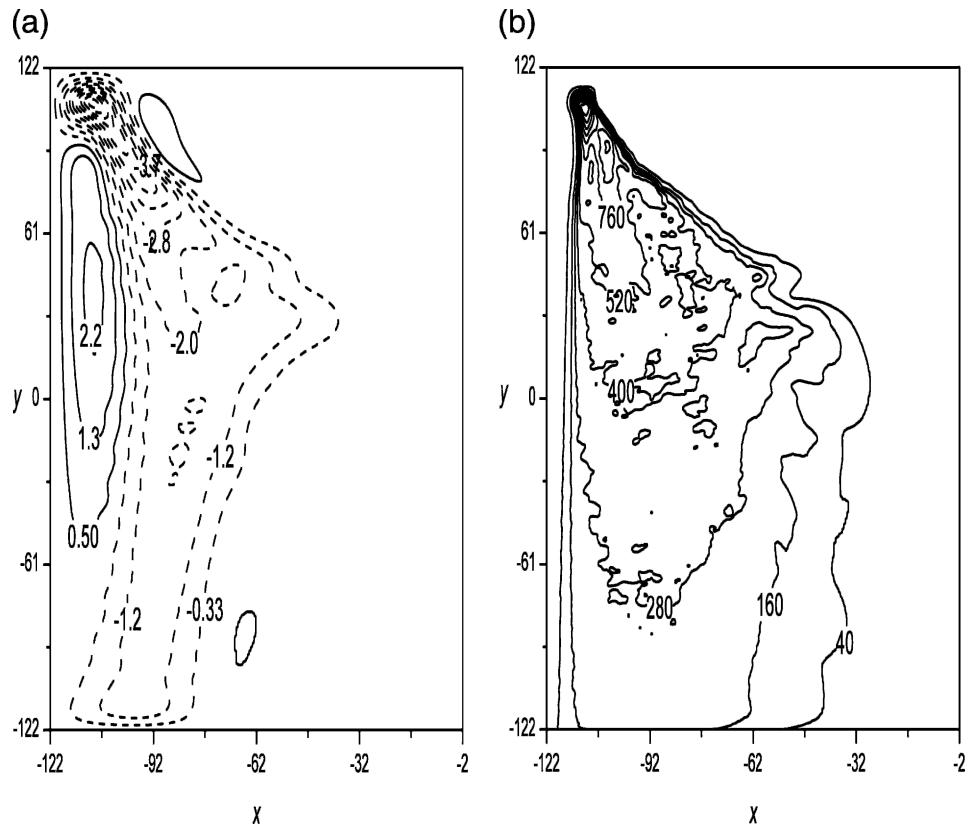
(a)

(b)

FIG. 4. Time-averaged (a) barotropic QG streamfunction $\overline{\psi}_{BT}(x, y)$ and (b) abyssal layer height $\overline{h^*}(x, y)$. The zonal extent of the domain has been restricted to $x_W < x < -2$ to facilitate greater detail being shown; $\overline{\psi}_{BT}$ is nondimensional but $\overline{h^*}$ is in meters. Negative and positive values of $\overline{\psi}_{BT}\overline{\psi}_{BT}$ are contoured with dashed and solid lines, respectively.

interior of the domain (i.e., for $x > -32$) where the flow is northward. The westward intensification seen in Fig. 4a is the result of β that inhibits the eastward (i.e., downslope) motion of the abyssal current (see, e.g., Anderson and Killworth 1979; Dewar 1987, among others; Part I) and is responsible for the westward propagation of Rossby waves in the QG layers. In addition, the westward intensification is further contributed to by the presence of the zonally sloping bottom, which acts like topographic β plane in the lower QG layer, and which also inhibits down slope abyssal motion as baroclinic instability occurs (Swaters 1991, 1998a; Reszka et al. 2002).

The elongated region of anticyclonic circulation, which is located adjacent to the western boundary, has a zonal width of about 300–400 km and extends from the southern edge of the strong localized cyclonic circulation in Ω_{down} all the way to $y = y_S$. The maximum in $\overline{\psi}_{BT}$ occurs in the anticyclonic gyre and has a value of about 3.0. Associated with this anticyclonic gyre is a weak northward barotropic QG current immediately adjacent to the western boundary, which is about 150

km wide and which, in dimensional magnitude, has a speed of about 0.6 cm s^{-1}. This is the same order of magnitude as the southward barotropic QG current speeds along the western flank of the broad cyclonic circulation cell, but an order of magnitude smaller than the barotropic QG current speeds in Ω_{down}.

The time-averaged abyssal height field shown in Fig. 4b exhibits a more or less monotonic decrease in the equatorward direction. The contour interval in Fig. 4b is 120 m. [The reason that the contours look a little noisy is a consequence of the fact that the friction parameter in (3.3) is rather small (i.e., $r_3 = 0.001$). Simulations done (not shown here) with a larger value of r_3 smooth out the contours.] The maximum abyssal height, which occurs at the center of Ω_{down}, is sharply peaked, and is given by, approximately, 2400 m (the scale depth of the water column is 5 km). The abyssal height falls off rather rapidly in the equatorward direction. This is a consequence of the fact, of course, that the source is localized but also follows from the conservation of PG PV on a β plane as shown in Part I.

There is a very slight upslope displacement, in the

equatorward direction, of the upslope grounding. This is also a consequence of the β effect as shown in Part I. The abyssal flow does spread eastward, or in the downslope direction, but this is arrested again because of β and also because the topography levels out. Numerical experiments (not presented here) showed that the abyssal current did continue to marginally spread zonally if one used, for example, the constant slope topography $h_B = -x + x_W$ but that, even so, the abyssal current did not reach the eastern boundary. Typical abyssal current speeds in Fig. 4b are about 3 cm s^{-1}.

Figures 5a–c show the zonally averaged ($\langle\ \rangle_x$) nondimensional QG barotropic streamfunction and dimensional abyssal layer height and the dimensional abyssal meridional transport, versus y, as computed from the time-averaged fields, respectively, and given by

$$\langle\overline{\psi}_{\mathrm{BT}}\rangle_x(y) \equiv \frac{1}{(x_E - x_W)}\int_{x_W}^{x_E}\overline{\psi}_{\mathrm{BT}}\,dx, \qquad (4.6)$$

$$\langle\overline{h^*}\rangle_x(y) \equiv s^*L\langle\overline{h}\rangle_x, \quad \langle\overline{h}\rangle_x \equiv \int_{x_W}^{x_E}\overline{h}\,dx\Big/\int_{x_W}^{x_E}\chi_h\,dx, \qquad (4.7)$$

and

$$\overline{\mathrm{Tr}}(y) \equiv (s^*U_*L^2)\int_{x_W}^{x_E}\overline{v}_3\overline{h}\,dx,$$

$$\overline{v}_3 \equiv \partial_x(\overline{\phi}_2 + \overline{h} + h_B)/(1 + s\beta y), \qquad (4.8)$$

respectively, where the $s^*U_*L^2 \simeq 3.8 \times 10^4$ m^3 s^{-1} = 0.038 Sv factor in (4.8) is the scaling for the transport [see (2.7)]. The subscript x associated with $\langle\ \rangle_x$ indicates that the averaging is done with respect to x and does not imply differentiation in this context. The averaging interval for the QG streamfunction is the entire zonal extent of the domain, while the averaging interval for the abyssal height is restricted to the support of h.

Figure 5a shows the generally negative QG streamfunction associated with the dominant cyclonic circulation in the upper QG layers. The minimum in $\langle\overline{\psi}_{\mathrm{BT}}\rangle_x$ is located at the y center of Ω_{down} and is a consequence of the downwelling associated with the formation of the abyssal water mass.

Figure 5b shows the monotonic decrease in $\langle\overline{h^*}\rangle_x$ in the equatorward direction. (The monotonic equatorward decrease is in sharp contrast to what is seen in the instantaneous field as will be discussed in section 4c.) The decrease is relatively rapid in the region $61 \lesssim y < 114.5$ (the northern edge of Ω_{down}), with the rate of decrease diminishing over the rest of the domain $y_S < y \lesssim 62$. As discussed above, the equatorward decrease in $\langle\overline{h^*}\rangle_x$ follows from the fact that the source is localized but is also a consequence of the conservation of PG
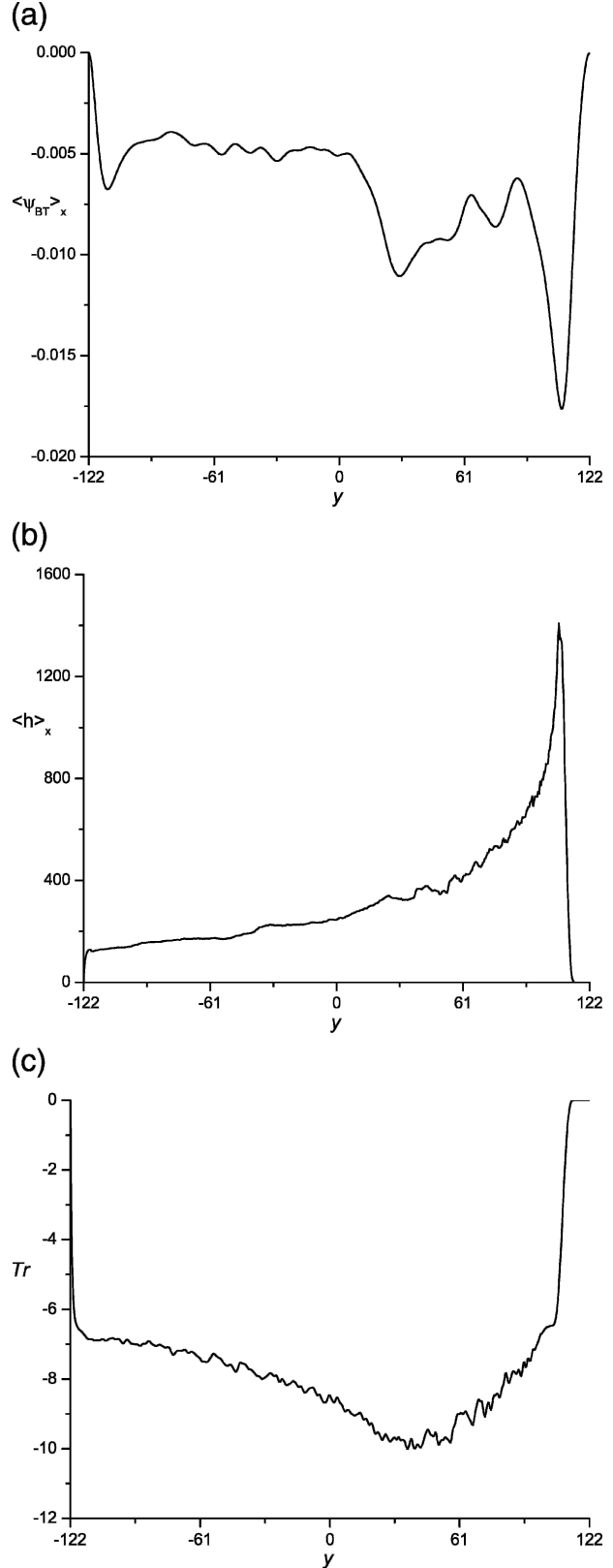

FIG. 5. Zonally averaged (a) barotropic QG streamfunction $\langle\overline{\psi}_{\mathrm{BT}}\rangle_x$ and (b) abyssal layer height $\langle\overline{h^*}\rangle_x$ and (c) the abyssal meridional transport $\overline{\mathrm{Tr}}$ vs y; $\langle\overline{\psi}_{\mathrm{BT}}\rangle_x$ is nondimensional, $\langle\overline{h^*}\rangle_x$ is in meters, and $\overline{\mathrm{Tr}}$ is in Sverdrups.

potential vorticity (PV) on a β plane as shown in Part I. Although it is difficult to see clearly in Fig. 5b, there is a smooth transition of $\langle \overline{h^*} \rangle_x \to 0$ as $y \downarrow y_S$ as a consequence of the upwelling zone and sponge layer in $y \in (-122, -112)$.

Figure 5c shows the meridional transport $\overline{\text{Tr}}$ in the abyssal layer (Sv). North of the source region Ω_{down}, there is, of course, no transport. South of the source region there is an increase in the equatorward mass transport that is maximum at $y \simeq 46$ (some 900 km equatorward of the southern edge of Ω_{down}) with a magnitude of about 10 Sv. The equatorward transport decreases slightly over the remaining region but the average equatorward transport is about 7.6 Sv. Numerical simulations (not shown here) with increased downward mass flux associated with Ω_{down} or increased topographic slope (resulting in a larger Nof speed) will increase the transport.

It was shown in Part I that, in the reduced gravity limit, the model would predict that the zonally averaged abyssal meridional transport would be constant with respect to y. The variability seen in Fig. 5c is a consequence of the baroclinic interactions between the abyssal layer and the overlying ocean. It is also important to note that the model does not contain any entrainment parameterizations that would certainly enhance the meridional abyssal transport that occurs. While not exactly constant with respect to y, it is nevertheless suggested that the relatively constant abyssal transport seen in Fig. 5c is not qualitatively inconsistent with the Stommel–Arons–Nof solution described in Part I.

Figures 6a–c show the meridionally averaged nondimensional QG barotropic streamfunction and dimensional total abyssal layer height, and the dimensional abyssal meridional mass flux, versus x, as computed from the time-averaged fields, respectively, and given by

$$\langle \overline{\psi}_{\text{BT}} \rangle_y (x) \equiv \frac{1}{(y_N - y_S)} \int_{y_S}^{y_N} \overline{\psi}_{\text{BT}} \, dy, \qquad (4.9)$$

$$(h_B^* + \langle \overline{h^*} \rangle_y)(x) \equiv s^*L(h_B + \langle \overline{h} \rangle_y),$$

$$\langle \overline{h} \rangle_y \equiv \int_{y_S}^{y_N} \overline{h} \, dy \Big/ \int_{y_S}^{y_N} \chi_h \, dy, \quad \text{and} \quad (4.10)$$

$$\langle \overline{v_3^* h^*} \rangle_y (x) \equiv (s^*LU_*) \int_{y_S}^{y_N} \overline{v_3} \overline{h} \, dy \Big/ \int_{y_S}^{y_N} \chi_h \, dy, \qquad (4.11)$$

respectively, where the $s^*LU_* \simeq 2.5 \text{ m}^2 \text{ s}^{-1}$ factor in (4.11) is the scaling for the mass flux [see (2.7)]. Again, the subscript y associated with $\langle \rangle_y$ indicates that the
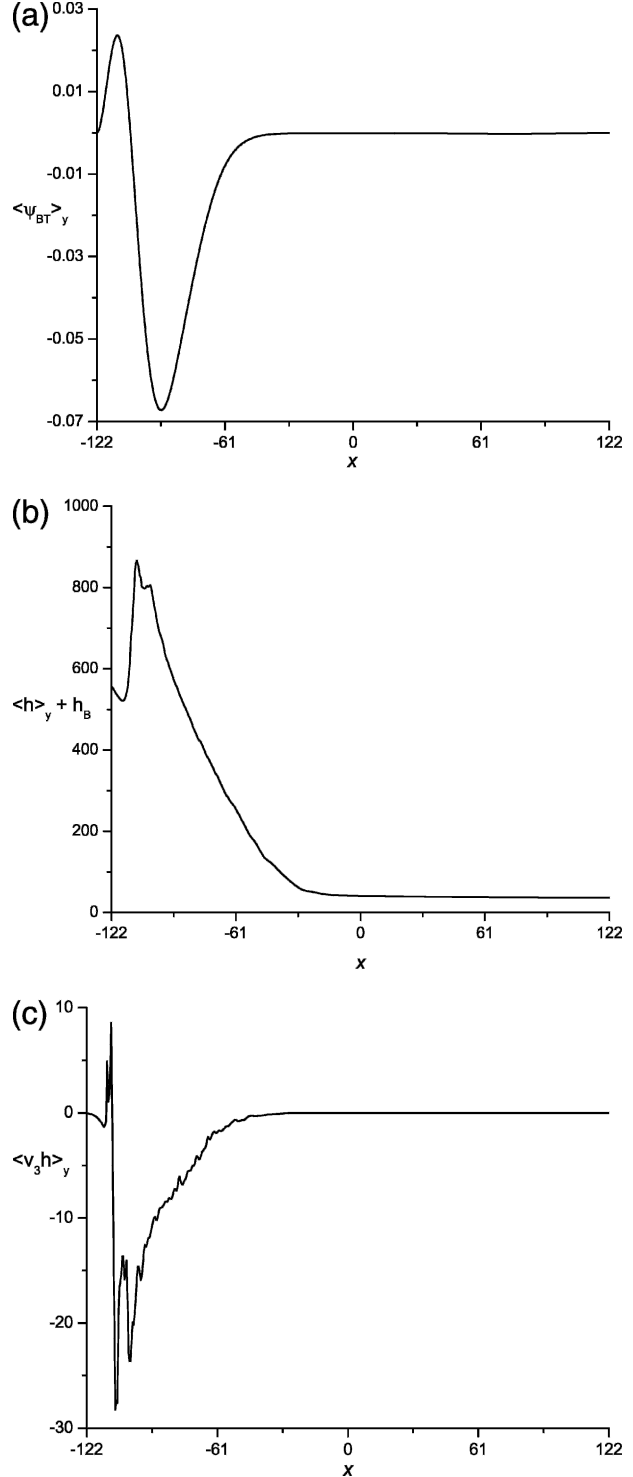

FIG. 6. Meridionally averaged (a) barotropic QG streamfunction $\langle \overline{\psi}_{\text{BT}} \rangle_y$, (b) total abyssal layer height $\langle \overline{h^*} \rangle_y + h_B^*$, and (c) meridional abyssal mass flux $\langle \overline{v_3^* h^*} \rangle_y$ vs x; $\langle \overline{\psi}_{\text{BT}} \rangle_y$ is nondimensional, the total height is in meters, and $\langle \overline{v_3^* h^*} \rangle_y$ is in meters squared per second.

averaging is done with respect to y and does not imply differentiation in this context. The averaging interval for the QG streamfunction is the entire meridional extent of the domain, while the averaging interval for the total abyssal height is restricted to the support of h. The total abyssal height corresponds to the full elevation above the reference depth of 5 km.

The averaged zonal structure associated with $\overline{\psi}_{BT}$ can be seen in Fig. 6a. The westward intensification is evident (this is why the truncated domain was used in Figs. 4a,b). As qualitatively described above in connection with Fig. 5a, one can see the narrow band of barotropic northward flow in the QG layers immediately adjacent to the western boundary, where $\partial_x(\langle\overline{\psi}_{BT}\rangle_y) > 0$, followed by a somewhat broader band of southward flow, where $\partial_x(\langle\overline{\psi}_{BT}\rangle_y) < 0$, followed again by another broad band of northward flow that rapidly decreases to zero as the interior of the domain is reached.

Figure 6b shows the height of the abyssal layer in meters above the reference depth of 5 km with the topography taken into account. The maximum in $\langle\overline{h^*}\rangle_y$ is located at $x \simeq -91$ and is given by approximately 425 m. The full zonal width of $\langle\overline{h^*}\rangle_y$ is about 1400 km, but the bulk of the abyssal water mass lies in a band that is about 900 km wide.

Figure 6c shows the meridionally averaged meridional transport in the abyssal layer (m^2 s^{-1}). The integral of $\langle\overline{v_3^* h^*}\rangle_y$ with respect to x over the entire domain is the same as the average of $\overline{\mathrm{Tr}}$, as shown in Fig. 5c, over the support of h. That is, the integral of $\langle\overline{v_3^* h^*}\rangle_y$ with respect to x, is the average meridional transport associated with the abyssal current and is given by approximately -7.6 Sv.

Another feature seen in Fig. 6c is that the meridionally averaged abyssal mass flux is not equatorward for every x. There is a narrow band of northward mass flux near the western boundary, or more precisely, associated with the abyssal height immediately adjacent to the upslope grounding since $\partial_x\overline{h} > 0$ in this region (the abyssal flow is geostrophically balanced). Additionally, however, there is a contribution to this northward flow due to the interaction with the overlying water column (recall the geostrophic pressure in the abyssal layer is $\phi_2 + h + h_B$) since there is a northward barotropic flow in the overlying QG layers. The maximum in $\langle\overline{\psi}_{BT}\rangle_y$ Fig. 6a (where the QG northward flow is zero) is located exactly at the maximum of $\langle\overline{v_3^* h^*}\rangle_y$ in Fig. 6c.

Thus, this simulation suggests that baroclinically coupled source-driven grounded abyssal currents over a sloping bottom have associated with them a barotropic northward flow on the western flank of the abyssal current. This supports the viewpoint that these equatorward flowing abyssal currents can have potentially sig-

nificant dynamical interactions with the surface intensified wind-driven boundary currents, the Gulf Stream for example, particularly at the crossover point as suggested by Spall (1996).

c. Instantaneous fields after 40 yr of integration

The instantaneous fields exhibit substantial variability as compared with the time-averaged fields. Figures 7a,b show contour plots of the nondimensional QG barotropic streamfunction ψ_{BT} and the dimensional abyssal height $h^* \equiv (s^*L)h$, respectively, at $t^* = 40$ yr in the simulation. As in Figs. 4a,b, since the instantaneous fields are essentially zero on the eastern side of the computational domain, only the western half of Ω is shown in order to show the detail more clearly. However, in contrast to Fig. 4a, the positive and negative values of ψ_{BT} in Fig. 7a are contoured with dashed and solid lines, respectively (it seemed more visually pleasing to do this), and the contour interval is ± 1.2. The contour interval for h^* in Fig. 7b is 400 m.

In examining Figs. 7a,b the first thing to notice is that in the region $y > 0$ there is a number of distinct cyclonic vortical structures in ψ_{BT} that are correlated with dome-like bolus features, or plumes, in h. These do not exist in the time-averaged fields in Figs. 4a,b. However, the anticyclonic circulation region immediately adjacent to the western boundary that gives rise to the northward barotropic flow along $x = x_W$ in the upper QG layers (which is in Fig. 4a), can also be seen in Fig. 7a.

Referring again to Fig. 7a, beginning immediately over the source region Ω_{down}, and extending in a southeast, or in an along- and downslope direction, there are four distinct cyclonic eddies that line up linearly (making about $-30°$ angle with the x axis along $y = 122$). There is also a fifth cyclonic eddy, or distinct local minimum in ψ_{BT}, which is located at $(x, y) \simeq (-80, -26)$. The eddies have typical radius on the order of 100–150 km (or, about, 7–10 internal deformation radii; recall $L \simeq 15$ km).

These five distinct features can also be clearly seen in Figs. 8a–c, which are the nondimensional zonally averaged QG barotropic streamfunction $\langle\psi_{BT}\rangle_x$, the dimensional abyssal height $\langle h^*\rangle_x \equiv (s^*L)\langle h\rangle_x$, and the dimensional abyssal meridional transport Tr, respectively, as determined by (4.6), (4.7), and (4.8), respectively, with the time-averaged fields replaced by the instantaneous fields. The five anomalies are labeled as A, B, C, D, and E, respectively, in Figs. 8a–c, with label A furthermost from the source region Ω_{down}. If the distance between the centers of the anomalies A and B is denoted as ΔAB (with similar definitions for the other anomalies), it follows that $\Delta AB \simeq 560$ km, $\Delta BC \simeq 360$ km, $\Delta CD \simeq$
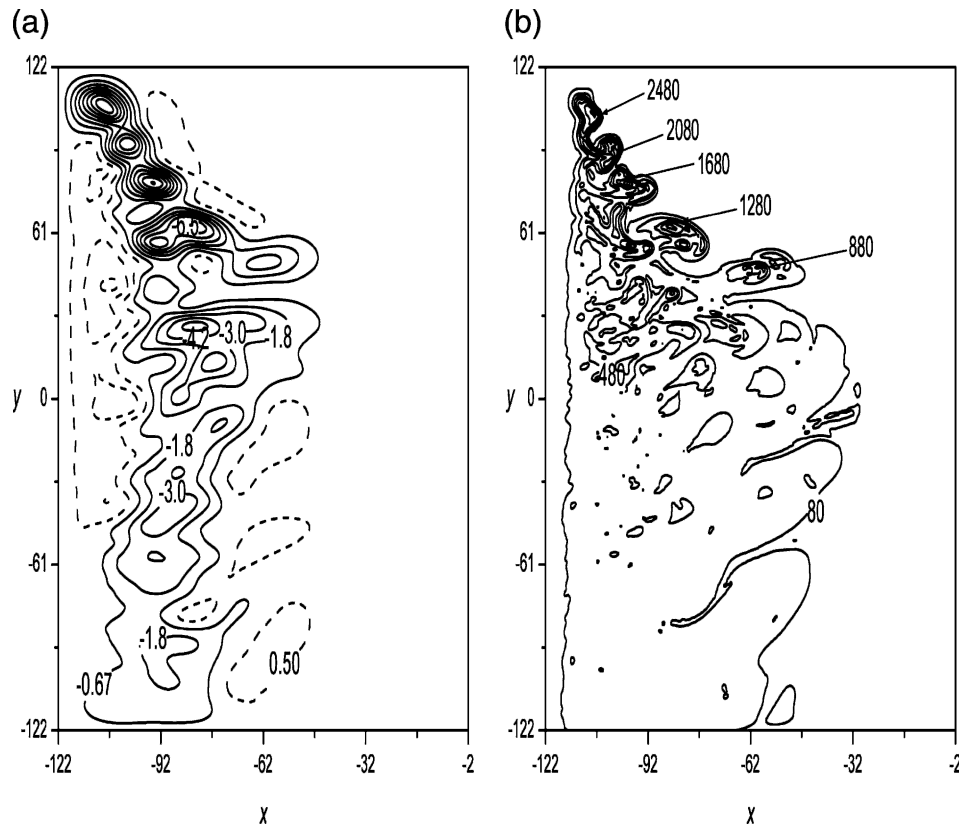
FIG. 7. (a) The barotropic QG streamfunction ψ_{BT} and (b) abyssal layer height h^* at $t^* = 40$ yr. The zonal extent of the domain has been restricted to $x_w < x < -2$ to facilitate greater detail being shown; ψ_{BT} is nondimensional and h^* is in meters. Negative and positive values of ψ_{BT} are contoured with solid and dashed lines, respectively. In (b), the local maxima in h^* associated with the individual plumes near Ω_{down} are marked.

250 km, and $\Delta DE \simeq 240$ km. A translation speed will be established for these anomalies shortly.

In Fig. 7b the point maximums in the height of the abyssal layer in the individual plumes near Ω_{down} have been labeled in meters. Figures 7b and 8b suggest that the maximum height of the abyssal anomalies associated with the cyclonic eddies in the QG layer decrease with increasing distance from Ω_{down}. Note that the maximum heights shown in Fig. 7b will not be the same as the heights computed for Fig. 8b since the heights in Fig. 7b are point values while those in Fig. 8b are zonally averaged over the support of h. The formation of a "mushroom" dipole structure can be clearly seen in the interior of the abyssal plumes in Fig. 7b.

Figure 8c is a graph of the instantaneous meridional transport (Sv) at $t^* = 40$ yr in the simulation. The abyssal height anomalies A, B, C, D, and E are marked. Associated with these anomalies is a local maximum in the equatorward abyssal transport. The local maxima in the equatorward abyssal transport are significant in comparison with the time-averaged results. In Fig. 8c there are abyssal anomalies that have transports greater

than 15 Sv, while the time-averaged transport, as seen in Fig. 5c, is never more than about 10 Sv.

The difference between the instantaneous and the time-averaged fields, as shown in Figs. 8 and 5, respectively, is striking. Whereas, for example, the meridional structure of $\langle \overline{h} \rangle_x$, as shown in Fig. 5b, exhibits a more-or-less smooth monotonic decrease in the equatorward direction, the presence of the abyssal height anomalies associated with the plumes or boluses is quite evident in Fig. 8b.

If a movie is made, in which the individual frames correspond to Fig. 8b plotted for each archived time step, the peaks in Fig. 8b move continuously equatorward, diminishing in amplitude as y decreases, until the peaks are absorbed into the relatively unchanging abyssal height region, approximately, $y_s < y \lesssim 0$. Similarly, for a movie made of individual frames corresponding to Fig. 8a plotted for each archived time step, the peaks and troughs in Fig. 8a move continuously equatorward, but while they do diminish in amplitude, they do not disappear altogether and there is continued spatial variability in the domain. This can be seen in Fig. 7a, for the
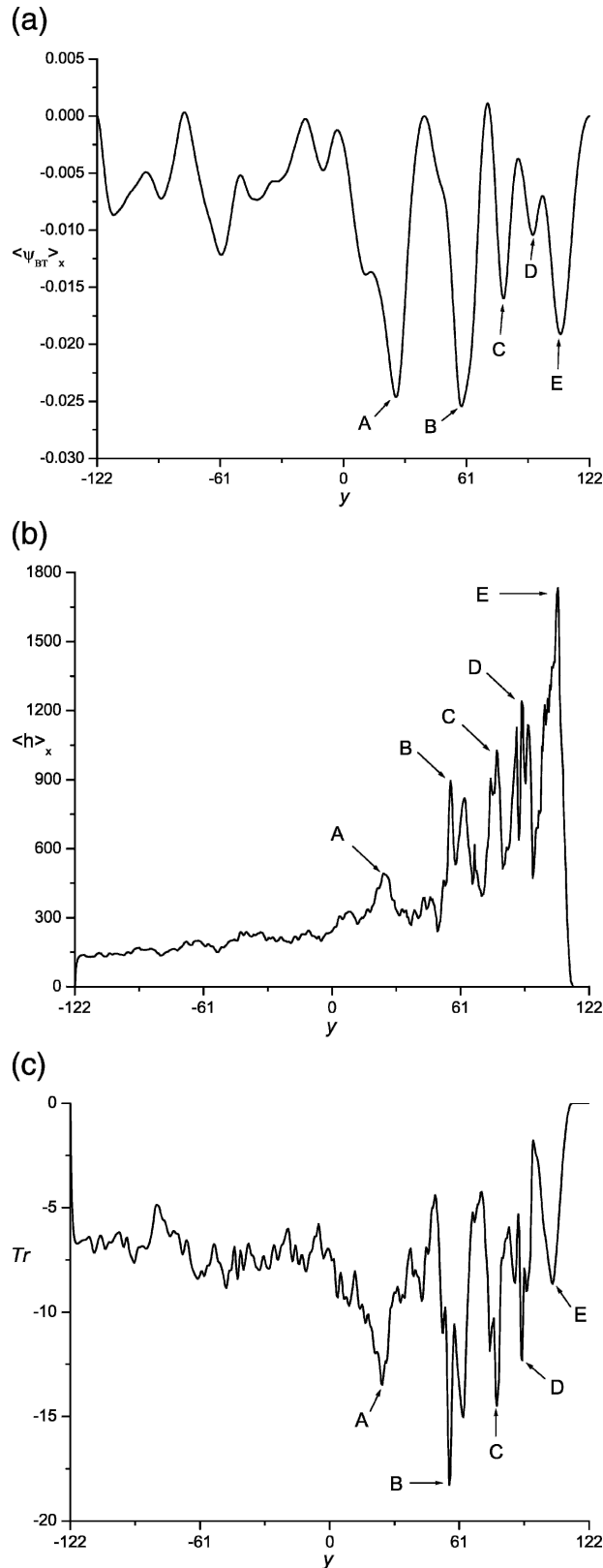
FIG. 8. Zonally averaged (a) barotropic QG streamfunction $\langle\psi_{BT}\rangle_x$ and (b) abyssal layer height $\langle h^*\rangle_x$ and (c) the abyssal meridional transport Tr vs y at $t^* = 40$ yr; $\langle\overline{\psi}_{BT}\rangle_x$ is nondimensional, $\langle h^*\rangle_x$ is in meters, and Tr is in Sverdrups. The points labeled A, B, C, D, and E in (a), (b), and (c) are correlated.

time-averaged barotropic QG streamfunction, in which there are still a number of closed contours in ψ_{BT} in the southern half of the domain. Notwithstanding this variability, the time-averaged fields give rise to an upper layer barotropic circulation pattern as seen in Fig. 4a.

For a movie made of the 2D fields ψ_{BT} and h, in which the individual frames correspond to Figs. 7a,b, respectively, plotted for each archived time step, the cyclonic cells in Fig. 7a are seen to amplify over Ω_{down} and subsequently move in the southeast direction and then eventually move in a south to southwest direction, all the while diminishing in amplitude. The corresponding movie for the abyssal height h (as shown in Fig. 7b) shows the formation of the abyssal water mass in Ω_{down} from which the plumes or boluses emerge, which move in the down- and along-slope direction, diminishing in amplitude and eventually being absorbed into the background abyssal water mass as described above. Implicit in these remarks is the idea that there is a periodic cycle occurring in the source region associated with the formation and intensification of the localized cyclonic circulation in the upper layer and subsequent shedding of the eddy. This is indeed the case.

Although it cannot be discerned from Figs. 7 and 8 directly, what is occurring in the simulation (and will be argued based on a power spectrum momentarily) is as follows. Once abyssal water production has started in the source region, it does not flow away from Ω_{down} in a steady laminar manner in a rectilinear along-slope (equatorward) direction. What happens is that, initially, the abyssal water mass accumulates in the immediate neighborhood of Ω_{down}. The downwelling associated with the abyssal water formation, through baroclinic PV stretching, leads to localized spinup in the overlying ocean, that is, the development of a localized cyclonic eddy. The localized low pressure anomaly in the overlying water column is phase locked with the localized abyssal height anomaly, as is suggested by the Mory–Stern isolation constraint (see Mory 1985; Mory et al. 1987; Swaters and Flierl 1991; Swaters 1998b). Heuristically, the localized low pressure eddies in the overlying water column help to hold up the abyssal height anomalies (see also Lane-Serff and Baines 1998, 2000; Etling et al. 2000). Once a certain volume or height threshold is obtained, however, the coupled abyssal water mass and localized cyclonic eddy breaks free from Ω_{down} and begins to propagate more-or-less equatorward (or more precisely in the along-slope direction), but does so in such a manner that a continuous, if instantaneously highly spatially and temporally variable, abyssal current will be formed, as shown in Figs. 7 and 8.

However, as has been shown in Part I (see also Swa-

ters 1991, 1998a), the abyssal current so formed is baroclinically unstable (even with β present). The baroclinic instability manifests itself in the abyssal current by the formation of preferentially amplifying perturbations on the downslope grounding of the abyssal current that evolve into downslope propagating abyssal plumes or boluses. The spatial asymmetry (neither varicose nor sinuous) of the perturbations is a distinguishing characteristic of the baroclinic destabilization theory described in Part I for grounded abyssal currents. The available gravitational potential energy of the downslope plumes and boluses is transferred into upper layer kinetic energy that is organized as along-slope (in this case equatorward) propagating topographic Rossby waves. These plumes can be seen in Fig. 7b, and the associated cyclonic cells in Fig. 7b are appropriately superimposed topographic Rossby waves. The phase locking and propagation that occur for the abyssal plumes or boluses and the QG cyclonic eddies is a result of the underlying baroclinic instability; that is, energy transfer between the abyssal current and overlying water column.

Further evidence that baroclinic instability is occurring in this simulation is that, considering (for the moment only) the sloping bottom as a topographic β plane in the QG layers' PV equations, so that westward in this context is in the direction of decreasing y, there is a westward phase shift with respect to height between the anomalies in ψ_{BT} and the geostrophic pressure in the abyssal layer given by $\phi_2 + h + h_B$ (not shown here). A remnant, however, can be seen of this property in Figs. 8a,b in which the individual peaks (not troughs) associated with A, B, C, D, and E in Fig. 8a are displaced slightly to the left of the local peaks in Fig. 8b. (Although it is difficult to see, the y coordinates of the local ψ_{BT} minimums in Fig. 8a are, in fact, displaced slightly to the right of the y coordinates of the h maximums in Fig. 8b. They do not exactly line up.)

The downslope propagation of the plumes (i.e., the baroclinic instability) does not, however, proceed unabated. The downslope motion is arrested for a number of reasons. First, there is the effect of the background topographic vorticity gradient, which acts to limit the across-slope motion associated with topographic Rossby waves (in exactly the same manner as β acts to limit the meridional motion of the planetary Rossby wave; see Pedlosky 1987).

Second, the presence of β itself will induce the real westward propagation (i.e., in the direction of decreasing x) and dispersion of the cyclonic anomalies in the overlying ocean seen in Fig. 8a (via the mechanism of planetary Rossby waves) and in the grounded abyssal anomalies (via the finite-amplitude mechanism of the

planetary shock wave balance; see Anderson and Killworth 1979; Dewar 1987, among others; Part I).

Over the full meridional extent of the computational domain, all of these effects are occurring. The role of β becomes increasingly important the further equatorward the abyssal current flows (it is a cumulative effect in this respect) and helps to maintain the westward intensification seen in Figs. 4 and 7. In addition, it is the strongly dispersive effect of β (and not, e.g., friction) that is responsible for loss of distinct local minimums associated in the cyclonic cells in the southward direction and the "smearing out" of the local maximums in the abyssal height that is seen in Figs. 7a,b. This loss of coherency in the plumes and upper layer cyclonic cells is not seen in numerical simulations without β (Swaters 1998a).

The periodicity associated with the formation and shedding of the cyclonic eddies in the upper layer and abyssal boluses or plumes can be seen in a time series of the minimum in the upper layer barotropic streamfunction, denoted as $\psi_{BT}|_{min}$. Figures 9a and 9b show graphs of $\psi_{BT}|_{min}$ versus the dimensional integration time t^* in years over the entire integration period $0 \le t^* \le 40$ yr and a closeup over the last five years of the numerical integration $35 \le t^* \le 40$ yr ($\psi_{BT}|_{min}$ has been computed every 12 days for Fig. 9). The individual oscillations can be clearly seen in Fig. 9b while Fig. 9a shows that the underlying pattern, at least in amplitude, occurs over the entire numerical integration (even if the individual oscillations cannot be discerned in Fig. 9a). Figure 9c shows the power spectrum associated with $\psi_{BT}|_{min}$ with the mean removed as computed for the interval $10 \le t^* \le 40$ yr. The abscissa is frequency in units of cpy. There is a single dominant single peak at about 54 days. There is no spectral peak associated with a longer time modulation of the amplitude of the oscillations in $\psi_{BT}|_{min}$.

However, the power spectra (not shown here) produced from a time series of the maximum in the abyssal layer height also had significant peaks at 149 and 185 days. The power spectra (not shown here) produced from a time series of the maximum in the zonally averaged abyssal layer height (i.e., the time series produced by the maximum in Fig. 8b as determined every 12 days) is identical to Fig. 9c but does show some variability at the first harmonic at 27 days.

Numerical experiments showed that the frequency associated with the spectral peak seen in Fig. 9c was an increasing function of magnitude of the downwelling volume flux in Ω_{down}. For example, keeping all other parameters the same but doubling $\mathcal{H}_{down}$ to 12 (corresponding to doubling the downwelling volume flux in Ω_{down} to 11.2 Sv) leads to a dominant single peak in the power spectrum for $\Omega_{BT}|_{min}$ at about 34 days. Similarly,
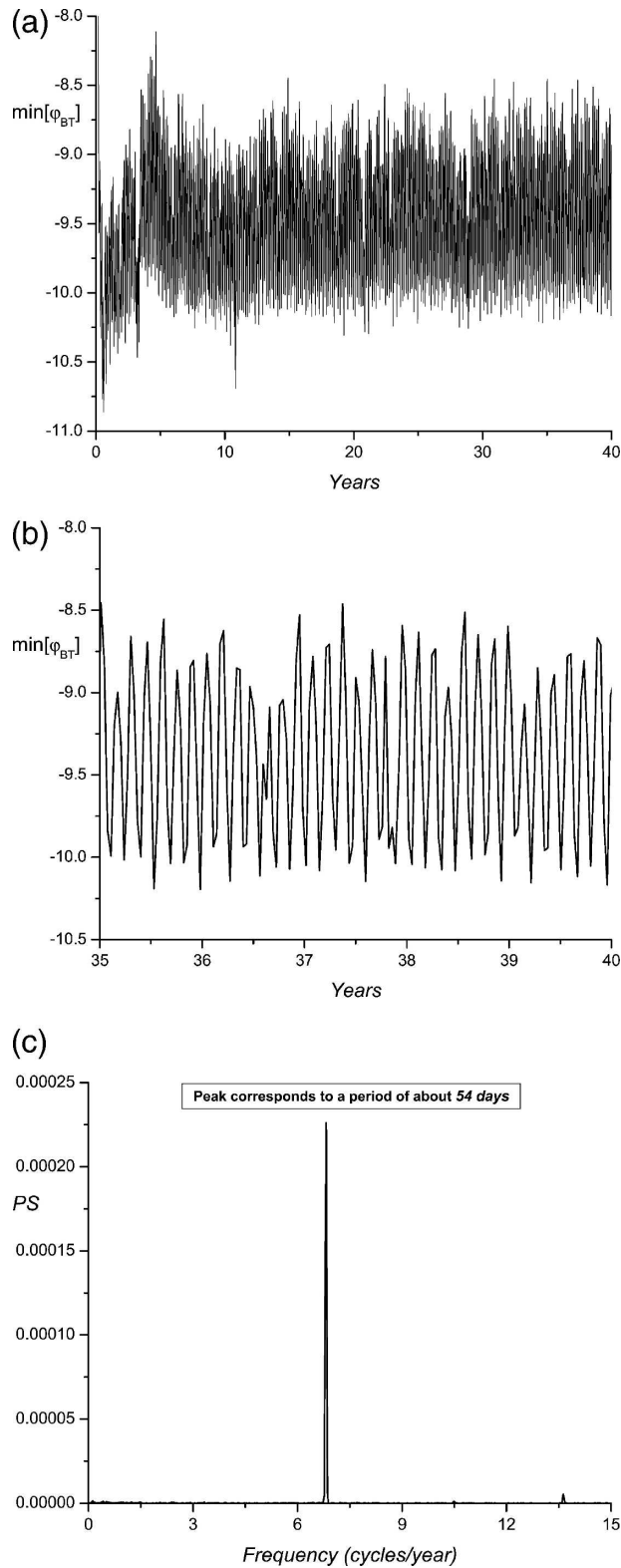
FIG. 9. (a) The $\psi_{BT}|_{min}$ vs integration time for the interval $0 \leq t^* \leq 40$ yr. (b) Close-up of $\psi_{BT}|_{min}$ over the last 5 yr of the integration. (c) Power spectrum of $\psi_{BT}|_{min}$ (with the linear trend removed) vs the frequency (in cycles per year so that the period is in units of inverse frequency).

keeping all other parameters the same but halving $\mathcal{H}_{down}$ to 3 (corresponding to halving the downwelling volume flux in Ω_{down} to 2.8 Sv) leads to a dominant single peak in the power spectrum for $\psi_{BT}|_{min}$ at about 72 days. Thus a doubling or halving of the downwelling volume flux leads to, respectively, a 33% increase or 35% decrease in the frequency associated with the spectral peak in the power spectrum for $\psi_{BT}|_{min}$ as compared with that seen in Fig. 9c. Clearly, this is not a purely linear response. A forthcoming contribution will examine this process in more detail. For the purposes of the present discussion, it suffices to remark that a steady localized source can result in a highly variable (but localized) baroclinic response with a sharply peaked power spectrum.

It follows from Fig. 9c that the A, B, C, D, and E minimums (maximums) in $\Psi_{BT}(h)$ that are seen in Fig. 8a (Fig. 8b), which correlate with the centers of the cyclonic eddies (plumes) seen in Fig. 7a (Fig. 7b), were formed in Ω_{down} about every 54 days. Based on the separation distances given previously for ΔAB, ΔBC, ΔCD, and ΔDE, this implies that the translation speeds of these anomalies are on the order of about 5–10 cm s^{-1}.

It is further suggested that the dynamical sequence described here of initial cyclogenesis (due to stretching), detachment, and phase locking with the abyssal boluses or plumes (which are formed because of baroclinic instability) is the mechanism responsible for the formation of mesoscale cyclonic eddies (with periods of a few days) in, for example, the Denmark Strait Overflow (Bruce 1995; Krauss and Käse 1998; Jungclaus et al. 2001). That is, it is suggested that the mechanism for cyclogenesis and detachment and propagation is a combination of the PV process proposed by Spall and Price (1998) and the Swaters (1991) baroclinic instability mechanism. The Spall and Price mechanism initiates cyclogenesis in the source region and the Swaters baroclinic instability mechanism leads to detachment from the source region and phase locking with the along-slope propagating abyssal plumes and boluses that are formed along the down slope grounding in the abyssal layer height.

5. Conclusions

This paper is a continuation of Part I in which a coupled QG–PG model was introduced to investigate the baroclinic evolution of meridionally flowing source-driven abyssal currents over sloping topography in a stratified β-plane basin. In Part I, the theoretical properties of the model were described. In this paper, a numerical simulation has been presented.

In summary, the time averaged abyssal current flows

equatorward, in the along-slope direction, with some zonal spreading that is arrested because of the background vorticity gradients (both β and topographic). The zonal average of the time-averaged abyssal height exhibits a monotonic decrease in the equatorward direction that is a consequence of the abyssal PG PV balance on a β plane. Typical abyssal equatorward velocities are about 3 cm s^{-1}. The zonally and time-averaged abyssal height is maximum in the source region with a thickness of about 1400 m. The meridionally averaged height of the zonally and time-averaged abyssal current away from the source region is about 300 m. The equatorward abyssal transport associated with the time averaged flow is about 8 Sv, and varies somewhat with respect to latitude. The maximum equatorward transport occurs just south of the source region and is about 10 Sv. Zonally, the abyssal current possesses both up- and downslope groundings or incroppings in the height field.

The time-averaged barotropic circulation pattern in the upper QG layers is mostly cyclonic and extends meridionally throughout the domain but is western intensified. Typical speeds associated with this circulation are about 0.6 cm s^{-1}. However, in the source region, the barotropic cyclonic circulation intensifies (due to stretching) and the barotropic current speeds increase to about 4 cm s^{-1}. There is also a region of barotropic anticyclonic circulation in the time-averaged upper QG layers that gives rise to a northward barotropic flow immediately adjacent to the western boundary that is about 150–200 km wide and has a speed of about 0.6 cm s^{-1}.

The instantaneous fields revealed pronounced baroclinic activity and time variability. Even though the downwelling that produces the abyssal current is steady, there is a very strong periodicity at 54 days in the flow near the source region. The periodicity is associated with cyclogenesis in the overlying water column, which occurs as a result of the stretching associated with the downwelling, and the subsequent shedding of the eddies from the source region. It was shown that the abyssal flow forms through a process of abyssal water mass accumulation and detachment in the source region that nevertheless results in a contiguous abyssal current. The abyssal water mass that is formed in the source region flows out of the source region as plumes that have associated with them relatively intense periodic cyclonic eddies, that extend throughout the water column, in the overlying QG layers. The eddies have a radius of about 100–150 km and have propagation speeds of about 5–10 cm s^{-1}.

There is a baroclinic transfer of gravitational potential energy from the downslope propagating abyssal plumes or boluses to the eddy field in the overlying ocean. The detached cyclones in the overlying water column are phase locked with the abyssal plumes and boluses that form because of baroclinic instability. Eventually, however, the downslope (i.e., eastward) motion is arrested because of the combined influences of the two background vorticity gradients and the flow becomes more oriented in the south-southwest direction and increasingly western intensified. The boluses associated with the plumes in the abyssal layer propagate southward and diminish in amplitude so that in the southern half of the domain the abyssal layer exhibits limited time variability. The eddy activity in the upper layers, while diminished, does not disappear altogether in the southern half of the domain, although when time-averaged, a coherent cyclonic circulation is generated as described above.

It was argued that the mechanism responsible for the formation of mesoscale cyclonic eddies in, for example, the Denmark Strait Overflow (Bruce 1995; Krauss and Käse 1998; Jungclaus et al. 2001) is a combination of the PV process proposed by Spall and Price (1998) and the Swaters (1991) baroclinic instability mechanism. That is, the Spall and Price mechanism initiates cyclogenesis and the Swaters baroclinic instability mechanism leads to detachment from the source region and phase locking with the propagating abyssal plumes and boluses that are formed along the downslope grounding.

This paper has raised a number of issues that should be examined further. In particular, it would be interesting to examine, using the coupled QG–PG model introduced here, the dynamical interaction of the abyssal current with the surface intensified wind-driven circulation. The dynamics of the crossover between equatorward deep western boundary currents and poleward wind–driven boundary currents is not fully understood.

Another aspect of the simulation described here is the time variability observed in the abyssal current. As is increasingly clear, time variability can have a profound influence on the baroclinic stability properties of abyssal and other currents (see, e.g., Pedlosky and Thomson 2003; Pavec et al. 2005; Ha and Swaters 2006). It would be interesting to consider this effect in the context of source-driven grounded abyssal currents. Another issue that needs a proper theoretical treatment is understanding the dynamical underpinnings associated with the very strong spectral peak in Fig. 9c.

REFERENCES

Anderson, D., and P. D. Killworth, 1979: Non-linear propagation of long Rossby waves. *Deep-Sea Res.,* **26,** 1033–1050.

Arakawa, A., 1966: Computational design for long term numerical integration of the equations of fluid motion: Two-dimensional incompressible flow. *J. Comput. Phys.,* **1,** 119–143.

Asselin, R. A., 1972: Frequency filter for time integrations. *Mon. Wea. Rev.,* **100,** 487–490.

Bruce, J. G., 1995: Eddies southwest of Denmark Strait. *Deep-Sea Res.,* **42,** 13–29.

Dewar, W. K., 1987: Planetary shock waves. *J. Phys. Oceanogr.,* **17,** 470–482.

Etling, D., F. Gelhardt, U. Schrader, F. Brennecke, G. Küihn, G. Chabert d'Hieres, and H. Didelle, 2000: Experiments with density currents on a sloping bottom in a rotating fluid. *Dyn. Atmos. Oceans,* **31,** 139–164.

Ha, S. J., and G. E. Swaters, 2006: Finite-amplitude baroclinic instability of time-varying abyssal currents. *J. Phys. Oceanogr.,* **36,** 122–139.

Holland, W. R., 1978: The role of mesoscale eddies in the general circulation of the ocean—Numerical experiments using a wind-driven quasi-geostrophic model. *J. Phys. Oceanogr.,* **8,** 363–392.

Hou, T. Y., and B. T. R. Wetton, 1992: Convergence of a finite difference scheme for the Navier-Stokes equations using vorticity boundary conditions. *SIAM J. Numer. Anal.,* **29,** 615–639.

Jungclaus, J. H., J. Hauser, and R. H. Käse, 2001: Cyclogenesis in the Denmark Strait overflow plume. *J. Phys. Oceanogr.,* **31,** 3214–3229.

Krauss, W., and R. H. Käse, 1998: Eddy formation in the Denmark Strait overflow. *J. Geophys. Res.,* **103,** 15 523–15 538.

Lane-Serff, G. F., and P. Baines, 1998: Eddy formation by dense flows on slopes in a rotating fluid. *J. Fluid Mech.,* **363,** 229–252.

——, and ——, 2000: Eddy formation by overflows in stratified water. *J. Phys. Oceanogr.,* **30,** 327–337.

LeBlond, P. H., H. Ma, F. Doherty, and S. Pond, 1991: Deep and intermediate water replacement in the Strait of Georgia. *Atmos.–Ocean,* **29,** 288–312.

Masson, D., 2002: Deep water renewal in the Strait of Georgia. *Estuarine, Coastal Shelf Sci.,* **54,** 115–126.

McWilliams, J. C., 1977: A note on a consistent quasigeostrophic model in a multiply connected domain. *Dyn. Atmos. Oceans,* **1,** 427–441.

Mory, M., 1985: Integral constraints on bottom and surface isolated eddies. *J. Phys. Oceanogr.,* **15,** 1433–1438.

——, M. E. Stern, and R. W. Griffiths, 1987: Coherent baroclinic eddies on a sloping bottom. *J. Fluid Mech.,* **183,** 45–62.

Nof, D., 1983: The translation of isolated cold eddies on a sloping bottom. *Deep-Sea Res.,* **30,** 171–182.

Orszag, S. A., and M. Israeli, 1974: Numerical simulation of viscous incompressible flows. *Annu. Rev. Fluid Mech.,* **6,** 281–318.

Pavec, M., X. Carton, and G. Swaters, 2005: Baroclinic instability of frontal geostrophic currents over a slope. *J. Phys. Oceanogr.,* **35,** 911–918.

Pedlosky, J., 1987: *Geophysical Fluid Dynamics.* 2d ed. Springer-Verlag, 710 pp.

——, and J. Thomson, 2003: Baroclinic instability of time dependent currents. *J. Fluid Mech.,* **490,** 189–215.

Reszka, M. K., G. E. Swaters, and B. R. Sutherland, 2002: Instability of abyssal currents in a continuously stratified ocean with bottom topography. *J. Phys. Oceanogr.,* **32,** 3528–3550.

Richardson, P. L., 1977: On the crossover between the Gulf Stream and the Western Boundary Undercurrent. *Deep-Sea Res.,* **24,** 139–159.

Spall, M. A., 1996: Dynamics of the Gulf Stream/deep western boundary current crossover. Part 1. Entrainment and recirculation. *J. Phys. Oceanogr.,* **26,** 2152–2168.

——, and J. F. Price, 1998: Mesoscale variability in Denmark Strait: The PV outflow hypothesis. *J. Phys. Oceanogr.,* **28,** 1598–1623.

Stommel, H., and A. B. Arons, 1960: On the abyssal circulation of the world ocean - I. Stationary flow patterns on a sphere. *Deep-Sea Res.,* **6,** 140–154.

Swaters, G. E., 1991: On the baroclinic instability of cold-core coupled density fronts on sloping continental shelf. *J. Fluid Mech.,* **224,** 361–382.

——, 1993: Nonlinear stability of intermediate baroclinic flow on a sloping bottom. *Proc. Roy. Soc. London A,* **442,** 249–272.

——, 1998a: Numerical simulations of the baroclinic dynamics of density-driven coupled fronts and eddies on a sloping bottom. *J. Geophys. Res.,* **103,** 2945–2961.

——, 1998b: Dynamics of radiating cold domes on a sloping bottom. *J. Fluid Mech.,* **364,** 221–251.

——, 2006: The meridional flow of source-driven abyssal currents in a stratified basin with topography. Part I. Model development and dynamical characteristics. *J. Phys. Oceanogr.,* **36,** 335–355.

——, and G. R. Flierl, 1991: Dynamics of ventilated coherent cold eddies on a sloping bottom. *J. Fluid Mech.,* **223,** 565–587.